Electronic and transport properties of T-graphene nanoribbon: Symmetry-dependent multiple Dirac points, negative differential resistance and linear current-bias characteristics

2014 EPL 107 37004

(http://iopscience.iop.org/0295-5075/107/3/37004)

A Letters Journal Exploring the Frontiers of Physics

August 2014

EPL, **107** (2014) 37004 www.epljournal.org
doi: 10.1209/0295-5075/107/37004

Electronic and transport properties of T-graphene nanoribbon: Symmetry-dependent multiple Dirac points, negative differential resistance and linear current-bias characteristics

C. J. Dai[1], X. H. Yan[1,2(a)], Y. Xiao[1] and Y. D. Guo[1,2]

[1] *College of Science, Nanjing University of Aeronautics and Astronautics - Nanjing 210016, PRC*
[2] *College of Electronic Science and Engineering, Nanjing University of Posts and Telecommunications Nanjing, 210046, PRC*

received 2 April 2014; accepted in final form 11 July 2014
published online 31 July 2014

PACS 73.22.-f – Electronic structure of nanoscale materials and related systems
PACS 73.63.-b – Electronic transport in nanoscale materials and structures
PACS 61.46.-w – Structure of nanoscale materials

Abstract – Based on the tight-binding method and density functional theory, band structures and transport properties of T-graphene nanoribbons are investigated. By constructing and solving the tight-binding Hamiltonian, we derived the analytic expressions of the linear dispersion relation and Fermi velocity of Dirac-like fermions for armchair T-graphene nanoribbons. Multiple Dirac points, which are triggered by the mirror symmetry of armchair T-graphene nanoribbons, are observed. The number and positions of multiple Dirac points can be well explained by our analytic expressions. Tight-binding results are confirmed by the results from density functional calculations. Moreover, armchair T-graphene nanoribbons exhibit negative differential resistance, whereas zigzag T-graphene nanoribbons have linear current-bias voltage characteristics near the Fermi level.

Introduction. – Graphene [1] has attracted much scientific interest for both the understanding of fundamental physics and promising future applications [2,3]. The unique electronic properties of graphene arise from the existence of Dirac cones, where the valence and conduction bands meet linearly at a single point in the momentum space, called Dirac point [2,4–6]. The linear dispersion relation around the Dirac point in the band structure (BS) of graphene is attributed to the graphene's honeycomb lattice [6]. Under this crystal symmetry, the electrons and holes in graphene can be described by Dirac equation and named Dirac fermions. Recently, it is reported that the Dirac points also exist in the two-dimensional carbon-based materials without honeycomb crystal symmetry [7–9], such as T-graphene [7], 6(H2),14,18-graphyne [8] and 6,6,12-graphyne [9].

Enyashin *et al.* [10] have studied systematically the stability, structural and electronic properties for twelve types of carbon allotropes. At almost the same time, Liu *et al.* [7] focused on T-graphene, which has a tetragonal symmetry. Buckled T-graphene is considered to be more stable than other carbon allotropes above 940 K [11,12] and it is also predicted to have Dirac-like fermions due to its linear dispersion and high Fermi velocity [13,14]. Also, they studied the buckled T-graphene nanoribbon and found similar Dirac-like fermion behaviour. Considering the unique properties of buckled T-graphene, we pay attention to another allotrope of carbon, planar T-graphene, which has a metallic BS [7]. Planar T-graphene is considered to be thermodynamically metastable due to the comparable formation energy of $-8.73\,\mathrm{eV/atom}$ [7]. Even in terms of free energy, planar T-graphene has a better thermodynamic stability than other carbon allotropes except graphene below 900 K.

As we know, it is important to know the structural dependence of electronic and transport properties for the application of nanostructures, since geometry structure is an important factor to tune the performance of device. In this paper, we studied BSs and transport properties of both TGNR with armchair edges (ATGNR) and TGNR with zigzag edges (ZTGNR) based on tight-binding (TB) method and density functional theory (DFT). Some interesting results, such as multiple Dirac points, are found.

(a) E-mail: xhyan@nuaa.edu.cn

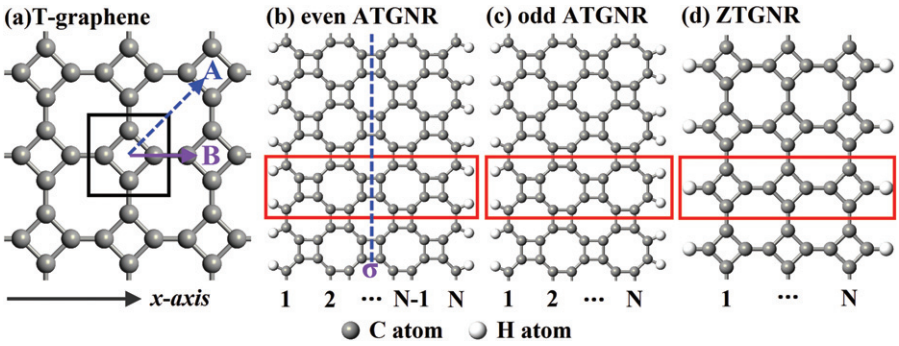

Fig. 1: (Colour on-line) Atomic model of T-graphene and TGNRs. (a) A T-graphene supercell. (b) Symmetric ATGNR (with even N). (c) Asymmetric ATGNR (with odd N). (d) ZTGNR.

Structural models of TGNRs. – The unit cell of a planar T-graphene is shown in fig. 1(a) (see the black square). It consists of four carbon atoms and the lattice constant is 3.46 Å, which is consistent with previous result [7,10]. After structural relaxation, the C-C bond in tetra-carbon ring is 1.468 Å while the one between nearest-neighboring tetra-rings is 1.383 Å. ATGNRs and ZTGNRs are obtained by cutting the T-graphene along A and B directions in fig. 1(a). The geometrical structures of ATGNR and ZTGNR are shown in figs. 1(b)–(d), where the red rectangles represent the unit cell of each TGNR. The ribbon width N denotes the number of carbon dimer chains for ATGNRs and the number of tetra-rings for ZTGNRs in each unit cell along the x-axis. As shown in figs. 1(b) and (c), ATGNRs with width N can be divided into two groups with respect to their symmetries: odd (even) N corresponds to asymmetric (symmetric) ATGNRs. Moreover, all TGNRs are saturated by Hydrogen atoms on the edges to eliminate the dangling bonds.

Computational details. – The BSs were calculated by means of both TB method and DFT method. In the calculations of transport properties, non-equilibrium Green's function (NEGF) method combined with DFT method is used to obtain the transmission spectrum and current-bias voltage (I-$V_{\rm bias}$) characteristics.

DFT and DFT/NEGF calculations are implemented with Atomistix ToolKit (ATK) [15,16]. Generalized gradient approximation (GGA) is used in the form of Perdew-Burke-Ernzerhof (PBE) exchange correlation functional [17]. The double-zeta polarized basis set of local orbitals is employed in all DFT calculations and the cutoff energy of numerical integration is set to be 150 Ry. The vacuum slab is more than 10 Å. Geometry optimization is implemented until the maximum-forces and maximum-stress on the irons were less than 0.005 eV/Å and 0.005 eV/Å^3, respectively. The first Brillouin zone is sampled with grid spacing less than 0.04 Å^{-1} in the Monkhorst-Pack scheme [18]. The I-$V_{\rm bias}$ characteristics are calculated by means of Landauer-Büttiker formula [19].

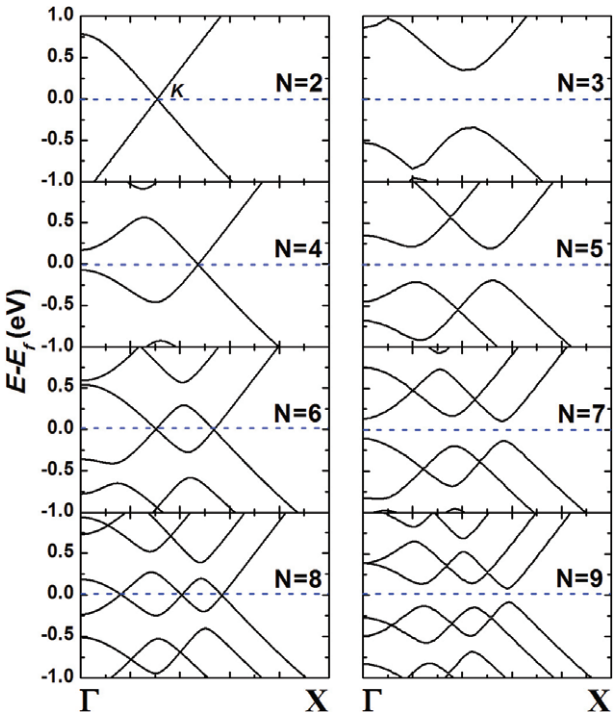

Fig. 2: (Colour on-line) DFT BSs for $N = 2$ up to 9 ATGNRs.

Band structures of ATGNRs from DFT. – Figure 2 shows DFT BSs of ATGNRs with different width (N = 2–9). The BSs near the Fermi level are quite different for symmetric (N is even) and asymmetric (N is odd) ATGNRs. In left column of fig. 2, the highest valence band and the lowest conduction band of symmetric ATGNRs meet at the Fermi level. More important, the dispersion of band is linear, which is a unique feature of massless Dirac fermions, *e.g.* graphene and topological insulator [6,20]. Moreover, as the width of nanoribbon increases, more Dirac points appear at the Fermi level. This is quite different from graphene. Comparing to symmetric ATGNRs, asymmetric ATGNRs show energy gaps at the Fermi level as shown in right column of fig. 2. In order to understand these DFT results, we next analytically show the mechanism behind the above behaviors based on the TB model.

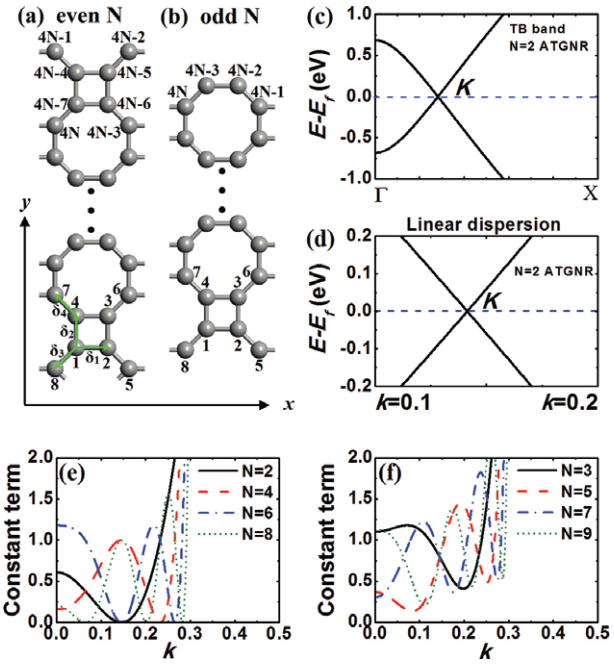

Fig. 3: (Colour on-line) The unit cells of (a) even N-ATGNR and (b) odd N-ATGNR. In (a), the nearest-neighboring vectors are marked with green. (c) BS from TB and (d) linear dispersion relation around Dirac point for $N = 2$ ATGNR. Constant terms for the eigenfunctions of $N = 2$, 4, 6, 8 and $N = 3$, 5, 7, 9 ATGNRs are shown in (e) and (f), respectively.

Band structures of ATGNRs from TB. – ATGNR is a quasi–one-dimensional (1D) structure and the unit cells of both symmetric and asymmetric ATGNRs are shown in fig. 3(a) and (b), respectively. The periodic boundary condition is taken along the x-axis and the lattice vector can be written as $\mathbf{a} = a\,(1,0)$, where $a = 4.89$ Å is the lattice constant. The reciprocal lattice vector is $\mathbf{b} = 2\pi/a\,(1,0)$ and we calculate the BS in the direction of $\Gamma(0,0)$-X $(\pi/a,0)$. The nearest-neighboring vectors in real space are given by

$$\begin{aligned} &\boldsymbol{\delta}_1 = l_1\,(1,0)\,, \quad \boldsymbol{\delta}_2 = l_1\,(0,1)\,, \\ &\boldsymbol{\delta}_3 = l_2\left(-\sqrt{2}/2, -\sqrt{2}/2\right), \quad \boldsymbol{\delta}_4 = l_2\left(-\sqrt{2}/2, \sqrt{2}/2\right), \end{aligned} \tag{1}$$

as shown in fig. 3(a). Here $l_1 = 1.468$ Å and $l_2 = 1.383$ Å are lengths of the two types of C-C bonds. Other neighboring vectors can be expressed by the negative ones of the vectors in eq. (1), such as $\boldsymbol{\delta}' = -\boldsymbol{\delta}_3$.

TB parameters can be obtained by many methods, such as quasi-atomic minimal basis set orbitals (QUAMBOs) approach. By considering the effect of local environment on the hopping integrals, QUAMBO-TB parameters can provide very exact BS for graphene-based systems [21–23]. Here, we focus on the effect of structural symmetry on the BSs and we need a simplified scheme of TB parameters to get some analytical results. In our TB model, we only consider the interaction of two nearest-neighboring atoms. In terms of the analytical formula of hopping integral in refs. [24,25], the C-C bonds of 1.468 Å and 1.383 Å in our work induce variations of about -6.5% and $+5\%$ in the hopping term of free graphene (2.7 eV), respectively. The hopping integrals of 1.468 Å and 1.383 Å C-C bonds are chosen to be $t_1 = 2.525$ eV and $t_2 = 2.835$ eV. The on-site energy of all carbon atoms is set to be zero.

We study the Hamiltonian of even N-ATGNRs first. According to ball and stick model shown in fig. 3(a), the TB Hamiltonian for an ATGNR with even N is given by

$$H_N = \begin{pmatrix} H_0 & H_c & 0 & \cdots & 0 \\ H_c^\dagger & H_0 & H_c & \cdots & 0 \\ 0 & H_c^\dagger & H_0 & \ddots & \vdots \\ \vdots & \vdots & \ddots & \ddots & H_c \\ 0 & 0 & \cdots & H_c^\dagger & H_0 \end{pmatrix}. \tag{2}$$

The block matrix H_c is a 8×8 sparse matrix, all elements in which equal zero except $H_c\,(6,5) = H_c\,(7,8) = t_1$. The block matrix H_0 has the form of

$$H_0 = \begin{pmatrix} 0 & t_1\beta & 0 & t_1 & 0 & 0 & 0 & t_2\alpha \\ t_1\beta^* & 0 & t_1 & 0 & t_2\alpha^* & 0 & 0 & 0 \\ 0 & t_1 & 0 & t_1\beta^* & 0 & t_2\alpha^* & 0 & 0 \\ t_1 & 0 & t_1\beta & 0 & 0 & 0 & t_2\alpha & 0 \\ 0 & t_2\alpha & 0 & 0 & 0 & 0 & 0 & t_1\beta \\ 0 & 0 & t_2\alpha & 0 & 0 & 0 & t_1\beta & 0 \\ 0 & 0 & 0 & t_2\alpha^* & 0 & t_1\beta^* & 0 & 0 \\ t_2\alpha^* & 0 & 0 & 0 & t_1\beta^* & 0 & 0 & 0 \end{pmatrix}. \tag{3}$$

Here, α and β are defined by

$$\begin{aligned} \alpha &= \exp\left(i\mathbf{k}\cdot\boldsymbol{\delta}_3\right) = \exp\left(i\mathbf{k}\cdot\boldsymbol{\delta}_4\right) = \exp\left(-0.4ik\pi\right), \\ \beta &= \exp\left(i\mathbf{k}\cdot\boldsymbol{\delta}_1\right) = \exp\left(0.6ik\pi\right), \end{aligned} \tag{4}$$

where $\mathbf{k} = 2\pi k/a\,(1,0)$ is the momentum vector, with $0 \le k \le 0.5$.

We can obtain an analytical energy band for the case of $N = 2$ based on eq. (2). The TB Hamiltonian for $N = 2$ is $H_2 = H_0$. By solving the eigenvalues of the matrix in eq. (3), the equations of two energy bands near Fermi level have the form of

$$\begin{aligned} E_\pm &= \pm\Big|-\frac{1}{2}t_1 \\ &\quad - \frac{1}{2}\sqrt{5t_1^2 + 4t_2^2 - 4\sqrt{t_1^4 + \Delta t_1^2 t_2^2 + 2t_1^2 t_2^2}}\Big|, \\ \Delta &= (\alpha^*\beta)^2 + (\alpha\beta^*)^2 = 2\cos\left(2k\pi\right), \end{aligned} \tag{5}$$

where Δ is the function of k. The energy bands in eq. (5) are shown in fig. 3(c). The position of Dirac point ($\mathbf{K}$ in fig. 3(c)) is consistent with the one shown in fig. 2. At the Dirac point, we have $E\,(\mathbf{K}) = 0$. By expanding the band equation in eq. (5) to the first order, *i.e.* $\mathbf{k} = \mathbf{K} + \mathbf{q}$ with $|\mathbf{q}| \ll |\mathbf{K}|$ and ignoring the high-order terms of $|\mathbf{q}|$, we can obtain the linear dispersion relation

$$E_\pm\left(\mathbf{q}\right) = \pm v_F\,|\mathbf{q}| = \pm\frac{2at_1^2t_2^2\pi}{\hbar\,|t_1|\,(t_1^2+t_2^2)}\sqrt{1-\frac{t_2^4}{4t_1^4}}\,|\mathbf{q}|\,, \tag{6}$$

where $\mathbf{q}$ is a small momentum measured from Dirac point $\mathbf{K}$. The energy bands of $N = 2$ ATGNR around $\mathbf{K}$ are magnified and shown in fig. 3(d), which exhibits an exact linear dispersion relation. v_F is Fermi velocity and its value is 5.1×10^6 m/s, which is close to the theoretical value of graphene [26].

For arbitrary even N, the eigenfunction of the matrix in eq. (2) can be written as

$$\left(f_{2N}E^{2N} + \cdots + f_2E^2 + f_1E + f_0\right) \times \left(f_{2N}E^{2N} + \cdots + f_2E^2 - f_1E + f_0\right) = 0,\ (f_{2N} \neq 0)\,. \quad (7)$$

This form is given out by computational software MATHEMATICA. We can obtain the analytical form of f_0 for arbitrary even N by using MATHEMATICA. When N is small, analytical forms can also be obtained for other coefficients, $f_i\,(i = 1, 2\cdots)$.

Near the Dirac point, *i.e.* $\mathbf{k} = \mathbf{K} + \mathbf{q}$ with $|\mathbf{q}| \ll |\mathbf{K}|$, the energy E satisfies the equation $E(\mathbf{k}) \simeq 0$. Expanding eq. (7) and only keeping terms linear in E and zeroth-order term in each bracket, we have

$$E_{\pm}(\mathbf{k}) = \pm\left|f_0/f_1\right|. \quad (8)$$

Based on this equation, we can obtain the linear dispersion relation by calculating f_0, f_1 and ignoring the high-order terms of $|\mathbf{q}|$. For $N = 4$ ATGNR, f_0 and f_1 have the forms of

$$f_0 = 4\pi t_1^4 t_2^4 \sqrt{1 - \left(\frac{t_2^2 - t_1^2}{2t_1^2}\right)^2}\,|\mathbf{q}|\,,\ f_1 = 4t_1^5 t_2^2 + 6t_1^3 t_2^4, \quad (9)$$

where $|\mathbf{q}|$ is the magnitude of $\mathbf{q}$. Thus we obtain

$$E_{\pm}(\mathbf{q}) = \pm v_F\,|\mathbf{q}| = \pm\left|\frac{4a\pi t_1^4 t_2^4}{\hbar\left(4t_1^5 t_2^2 + 6t_1^3 t_2^4\right)}\sqrt{1 - \left(\frac{t_2^2 - t_1^2}{2t_1^2}\right)^2}\right|\,|\mathbf{q}|\,. \quad (10)$$

From the above equation, we deduce the Fermi velocity $v_F \simeq 2.6 \times 10^6$ m/s.

We next explain why the number of Dirac points increases with N for even ATGNR. In eq. (7), the constant term can be written as

$$F_0^N = f_0^2 = \left\{t_2^N\left[\sum_{m=0}^{[N/4]} \lambda_m^m \left(t_2^2 - \Delta t_1^2\right)^{\frac{N}{2}-2m}\left(t_1^2\right)^{2m}\right]\right\}^2, \quad (11)$$

$$\lambda_j^i = \lambda_{j-1}^i - \lambda_{j-1}^{j-1} C_{N/2-2j+2}^{i-j+1}\ \ (j \geq 1, i \geq j, \lambda_0^n = 1\,(n \geq 0))$$

in which Δ has been given in eq. (5) and $C_{N/2-2j+2}^{i-j+1}$ is a combinatorial number. If F_0^N equals to zero, $E = 0$ is the eigenvalue of the Hamiltonian in eq. (2). This means valence and conduction bands meet at the vector $\mathbf{k}$, where $E(\mathbf{k}) = 0$. So we can determine the positions of Dirac points for arbitrary even N-ATGNR by the equation $F_0^N(k) = 0$. The curves of F_0^N for $N = 2$, 4, 6 and 8 ATGNRs are shown in fig. 3(e). The number and positions of the roots of $F_0^N(k) = 0$ are consistent with those of Dirac points in DFT BSs shown in fig. 2.

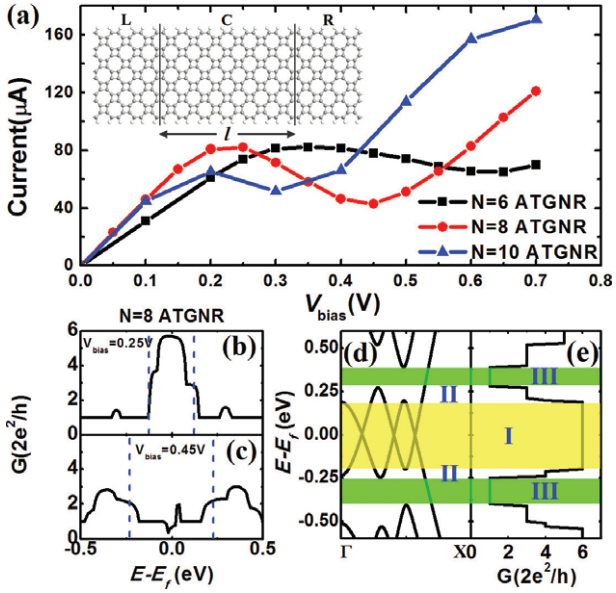

Fig. 4: (Colour on-line) (a) I-$V_{\rm bias}$ curves of $N = 6$, 8 and 10 ATGNR devices (see the inset). (b), (c) Transmission spectra under $V_{\rm bias} = 0.25$ V and 0.45 V for $N = 8$ ATGNR. The blue dashed lines in spectra represent the bias voltage windows. (d) BS and (e) zero-bias transmission spectrum of $N = 8$ ATGNR. According to the magnitude of conductance, three areas (I, II, III) are marked.

For an odd N-ATGNR (fig. 3(b)), the TB Hamiltonian (not given here) can be obtained easily and the eigenfunction of the Hamiltonian has the form

$$f_{4N}x^{4N} + \cdots + f_1x + f_0 = 0,\ (f_{4N} \neq 0)\,. \quad (12)$$

And the curves of f_0 for $N = 3$, 5, 7 and 9 are shown in fig. 3(f). f_0 never equals zero and there will be no bands appearing at the Fermi level, resulting in the band gaps.

The TB calculations indicate clearly that the occurrence of multiple Dirac points in even width ATGNRs is due to the mirror symmetry with respect to the midplane between two edges and the band gaps in odd width ATGNRs are induced by the structural broken-symmetry.

Transport properties of ATGNR devices. – In order to investigate the transport properties of ATGNRs under a bias voltage ($V_{\rm bias}$), the first-principle calculations of I-$V_{\rm bias}$ curves were performed by using a two-probe device (the inset of fig. 4(a)), where the left (L) and right (R) leads are semi-infinite ATGNRs and the length l of central region (C) is of 6 unit cells. The I-$V_{\rm bias}$ curves for $N = 6$, 8 and 10 ATGNRs are shown in fig. 4(a) and nearly regardless of the central region length l. These results suggest that negative differential resistance phenomenon (NDR) can exist in these devices. Taking the

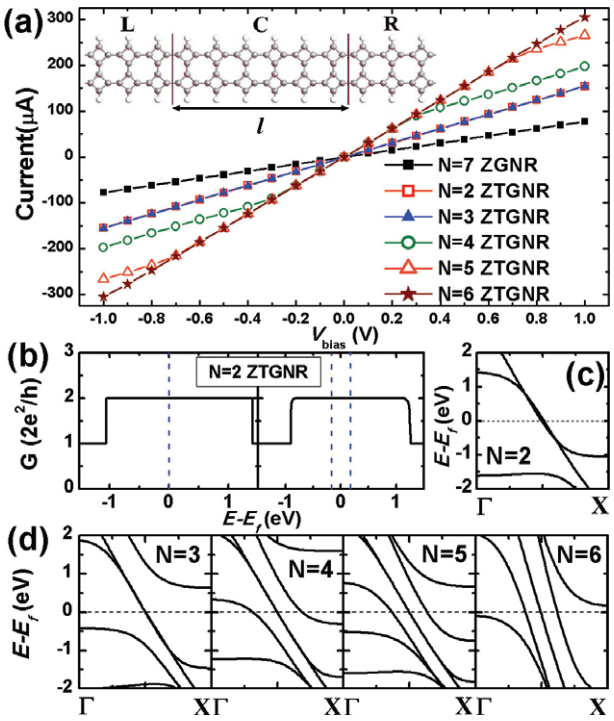

Fig. 5: (Colour on-line) (a) I-$V_{\rm bias}$ curves of $N = 2$, 3, 4, 5 and 6 ZTGNR devices (see the inset) and $N = 7$ ZGNR device. (b) Transmission spectra under $V_{\rm bias} = 0\,$V and $0.3\,$V for $N = 2$ ZTGNR device. The blue dashed lines represent the bias voltage windows. (c) BS of $N = 2$ ZTGNR. (d) BSs of $N = 3$, 4, 5 and 6 ZTGNRs.

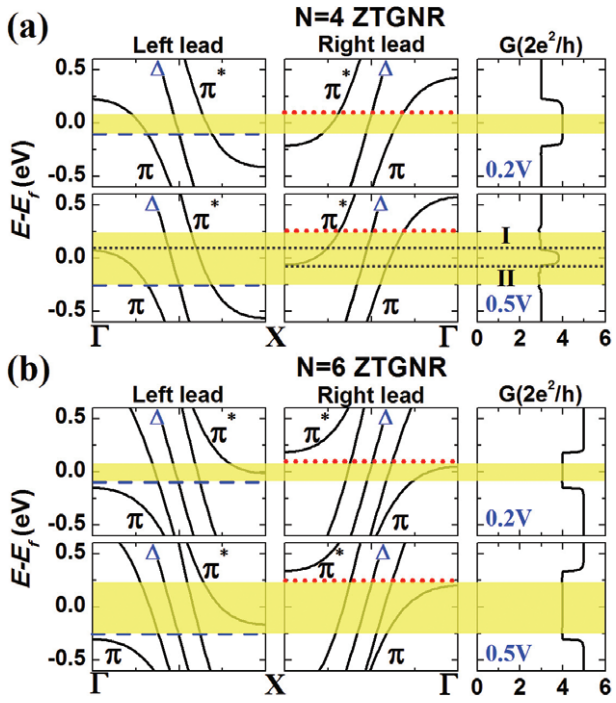

Fig. 6: (Colour on-line) BSs of two leads and transmission spectra under $V_{\rm bias}$ of $0.2\,$V and $0.5\,$V for (a) $N = 4$ ZTGNR and (b) $N = 6$ ZTGNR. The value of $V_{\rm bias}$ is represented using blue numbers. It is necessary to point out that the curve"Δ" in (a) and (b) contains two bands.

$N = 8$ ATGNR device as an example, current decreases when bias increases from $0.25\,$V to $0.45\,$V. From the $0.25\,$V and $0.45\,$V transmission spectra for $N = 8$ ATGNR device (figs. 4(b) and (c)), conductance at the Fermi level drops from about 5.6 G_0($G_0 = 2e^2/h$ is conductance quantum) at $0.25\,$V to about 1.0 G_0 at $0.45\,$V. This conductance reduction can be attributed to the BS (fig. 4(d)) and $0\,$V transmission spectrum (fig. 4(e)). Around the Fermi level (area I in fig. 4(d)), energy bands appear in this area for six times, providing a conductance of 6.0 G_0 (fig. 4(e)) in the same area. However, energy band appear only one time in area III in fig. 4(d) and contributes only conductance of 1.0 G_0 (fig. 4(e)). In area II, the conductance decreases from 6.0 G_0 to 1.0 G_0 as shown in fig. 4(e). This characteristic in band structure means that the number of electron tunneling channels reduces when the bias increases from $0.25\,$V to $0.45\,$V. So, current decreases in the $V_{\rm bias}$ range from $0.25\,$V to $0.45\,$V. This result suggests that NDR can be introduced in homogenous systems through a method of band structure engineering.

Transport properties of ZTGNR devices. – Similarly, two-probe devices of ZTGNRs (inset of fig. 5(a)) are constructed to study the transport behaviors of ZTGNRs under $V_{\rm bias}$. Figure 5(a) shows the I-$V_{\rm bias}$ curves of ZTGNRs with different widths and these curves are nearly independent on the length l. When $|V_{\rm bias}|$ is not very large, all I-$V_{\rm bias}$ curves are linear and have larger slopes than the I-$V_{\rm bias}$ curve of $N = 7$ zigzag graphene nanoribbon (ZGNR) in fig. 5(a). These results arise from the large conductance of ZTGNRs around the Fermi level. For example, $0\,$V and $0.3\,$V transmission spectra of $N = 2$ ZTGNR (fig. 5(b)) exhibit a conductance of 2 G_0, which can be further confirmed by the BS of $N = 2$ ZTGNR (fig. 5(c)). From the BSs of ZTGNRs in fig. 5(d), the larger slopes and linearity near $V_{\rm bias} = 0\,$V of I-$V_{\rm bias}$ curves can be understood.

When $|V_{\rm bias}|$ increases, I-$V_{\rm bias}$ curves of $N = 2$, 3 and 6 ZTGNRs remain linear while that of $N = 4$ and 5 ZTGNRs exhibit bending at the critical $|V_{\rm bias}|$ ($V_{\rm c}$) of $0.3\,$V and $0.8\,$V, respectively. Taking the $N = 4$ and 6 ZTGNRs as examples, we discuss the origin of the difference between these two kinds of I-$V_{\rm bias}$ curves. Under certain $V_{\rm bias}$ of $0.2\,$V (smaller than $V_{\rm c}$ of $N = 4$ ZTGNR) and $0.5\,$V (larger than $V_{\rm c}$ of $N = 4$ ZTGNR), BSs of two leads and transmission spectra for $N = 4$ and 6 ZTGNR devices are shown in figs. 6(a) and (b). BS of left (right) lead is obtained by shifting the BS of corresponding ZTGNR with $-V_{\rm bias}/2$ ($V_{\rm bias}/2$) for that the chemical potential of left (right) lead is set to be $-V_{\rm bias}/2$ ($V_{\rm bias}/2$) when we calculate the current under a certain $V_{\rm bias}$ by using ATK. In figs. 6(a) and (b), blue dashed (red dotted) line indicates the position of the chemical potential of left (right) lead and the yellow region is the integrating window for calculating current.

For $N = 4$ ZTGNR, the top of π band in left lead is higher than the chemical potential of right lead and the

bottom of π^* band in right lead is lower than the chemical potential of left lead when $V_{\rm bias}$ is 0.2 V, as shown in fig. 6(a). So under $V_{\rm bias}$ of 0.2 V, conductance is always 4 G_0 in the integrating window (0.2 V transmission spectrum in fig. 6(a)). However, the top (bottom) of π (π^*) band in left (right) lead locates in the integrating window when $V_{\rm bias}$ is 0.5 V, resulting in a conductance reduction in area I and II in the 0.5 V transmission spectrum (fig. 6(a)). Due to the conductance reduction in the integrating window, the rate of current increasing becomes smaller when $|V_{\rm bias}|$ increases beyond the $V_{\rm c}$, leading to the bending. For $N = 6$ ZTGNR (fig. 6(b)), the π (π^*) band in left (right) lead keeps out of the integrating window when $|V_{\rm bias}|$ increases, resulting in an unchanged conductance of 4 G_0 in the integrating window (0.2 V and 0.5 V transmission spectra in fig. 6(b)). The constant conductance of 4.0 G_0 provides a linear current increasing for $N = 6$ ZTGNR when $|V_{\rm bias}|$ increases, as shown in fig. 5(a).

Conclusion. – In conclusion, the band structures of ATGNRs exhibit a dependence on the mirror symmetry of the ribbon. Dirac-like fermions are found to exist in the symmetric ATGNRs while asymmetric ATGNRs have energy gaps in the band structures. Furthermore, the number and positions of Dirac points for arbitrary even width ATGNR are determined by the constant term of the eigenfunction of the Hamiltonian. The example of ATGNRs indicates that a large number of low-dimensional carbon-based materials with unique properties similarly to graphene await discovery and investigation. NDR phenomenon and linear I-$V_{\rm bias}$ characteristic are found to exist in the two-probe devices constructing from ATGNRs and ZTGNRs, respectively. Both these properties may play important role in the application of TGNRs in future.

* * *

This work was supported by the National Natural Science Foundation of China (NSFC51032002, NSFC11247033, NSFC11374162 and NSFC11347129), the key project of National High Technology Research and Development Program ("863" Program) of China (2011AA050526), the Science and Technology Support Plan of Jiangsu Province (BE2011191).

REFERENCES

[1] Novoselov K. S., Geim A. K., Morozov S. V., Jiang D., Zhang Y., Dubonos S. V., Grigorieva I. V. and Firsov A. A., *Science*, **306** (2004) 666.

[2] Novoselov K. S., Geim A. K., Morozov S. V., Jiang D., Katsnelson M. I., Grigorieva I. V., Dubonos S. V. and Firsov A. A., *Nature*, **438** (2005) 197.

[3] Zhang Y., Tan Y.-W., Stormer H. L. and Kim P., *Nature*, **438** (2005) 201.

[4] Geim A. K. and Novoselov K. S., *Nat. Mater.*, **6** (2007) 183.

[5] Geim A. K., *Science*, **324** (2009) 1530.

[6] Castro Neto A. H., Guinea F., Peres N. M. R., Novoselov K. S. and Geim A. K., *Rev. Mod. Phys.*, **81** (2009) 109.

[7] Liu Y., Wang G., Huang Q., Guo L. and Chen X., *Phys. Rev. Lett.*, **108** (2012) 225505.

[8] Malko D., Neiss C. and Görling A., *Phys. Rev. B*, **86** (2012) 045443.

[9] Malko D., Neiss C., Viñes F. and Görling A., *Phys. Rev. Lett.*, **108** (2012) 086804.

[10] Enyashin A. N. and Ivanovskii A. L., *Phys. Status Solidi B*, **248** (2011) 1879.

[11] Kim B. G., Jo J. Y. and Sim H. S., *Phys. Rev. Lett.*, **110** (2013) 029601.

[12] Liu Y., Wang G., Huang Q., Guo L. and Chen X., *Phys. Rev. Lett.*, **110** (2013) 029602.

[13] Huang H., Li Y., Liu Z., Wu J. and Duan W., *Phys. Rev. Lett.*, **110** (2013) 029603.

[14] Liu Y., Wang G., Huang Q., Guo L. and Chen X., *Phys. Rev. Lett.*, **110** (2013) 029604.

[15] Brandbyge M., Mozos J.-L., Ordejón P., Taylor J. and Stokbro K., *Phys. Rev. B*, **65** (2002) 165401.

[16] Taylor J., Guo H. and Wang J., *Phys. Rev. B*, **63** (2001) 245407.

[17] Perdew J. P., Burke K. and Ernzerhof M., *Phys. Rev. Lett.*, **77** (1996) 3865.

[18] Monkhorst H. J. and Pack J. D., *Phys. Rev. B*, **13** (1976) 5188.

[19] Büttiker M., Imry Y., Landauer R. and Pinhas S., *Phys. Rev. B*, **31** (1985) 6207.

[20] Hasan M. Z. and Kane C. L., *Rev. Mod. Phys.*, **82** (2010) 3045.

[21] Yao Y. X., Wang C. Z., Zhang G. P., Ji M. and Ho K. M., *J. Phys.: Condens. Matter*, **21** (2009) 235501.

[22] Zhang G. P., Fang X. W., Yao Y. X., Wang C. Z., Ding Z. J. and Ho K. M., *J. Phys.: Condens. Matter*, **23** (2010) 025302.

[23] Fang X. W., Zhang G. P., Yao Y. X., Wang C. Z., Ding Z. J. and Ho K. M., *Phys. Lett. A*, **375** (2011) 3710.

[24] Ding J. W., Yan X. H., Cao J. X., Wang D. L., Tang Y. and Yang Q. B., *J. Phys.: Condens. Matter*, **15** (2003) L439.

[25] Flügge S., *Practical Quantum Mechanics*, Vol. **1** (Springer, New York) 1974.

[26] Wallace P. R., *Phys. Rev.*, **71** (1947) 622.